Spin-momentum locked polariton transport in the chiral strong coupling regime

Thibault Chervy,[1] Stefano Azzini,[1] Etienne Lorchat,[2] Shaojun Wang,[3] Yuri Gorodetski,[4] James A. Hutchison,[1] Stéphane Berciaud,[2] Thomas W. Ebbesen,[1] and Cyriaque Genet[1]

[1] *ISIS & icFRC, Université de Strasbourg and CNRS, UMR 7006, F-67000 Strasbourg, France*
[2] *Université de Strasbourg, CNRS, IPCMS, UMR 7504, F-67000 Strasbourg, France*
[3] *Dutch Institute for Fundamental Energy Research, Eindhoven, The Netherlands*
[4] *Mechanical Engineering and Mechatronics Department and Electrical Engineering and Electronics Departement, Ariel University, Ariel 40700, Israel*

(Dated: January 30, 2017)

We demonstrate room temperature chiral strong coupling of valley excitons in a transition metal dichalcogenide monolayer with spin-momentum locked surface plasmons. In this regime, we measure spin-selective excitation of directional flows of polaritons. Operating under strong light-matter coupling, our platform yields long-lived coherences, enabling us to generate entangled counter-propagating flows of chiral polaritons. Our results reveal the rich and easy to implement possibilities offered by our system in the context of quantum coherent control.

arXiv:1701.07972v1 [cond-mat.mtrl-sci] 27 Jan 2017

Optical spin-orbit (OSO) interaction couples the polarization of a light field with its propagation direction [1]. An important body of work has recently described how OSO interactions can be exploited at the level of nano-optical devices, involving dielectric [2–5] or plasmonic architectures [6–9], all able to confine the electromagnetic field below the optical wavelength. Optical spin-momentum locking effects have been used to spatially route the flow of surface plasmons depending on the spin of the polarization of the excitation beam [10] or to spatially route the flow of photoluminescence (PL) depending on the spin of the polarization of the emitter transition [11]. Such directional coupling, also known as chiral coupling, has been demonstrated in both the classical and in the quantum regimes [12, 13]. Chiral coupling opens new opportunities in the field of light-matter interactions with the design of non-reciprocal devices, ultrafast optical switches, non destructive photon detector, and quantum memories and networks (see [14] and references therein).

In this letter, we propose a new platform consisting of spin-polarized valleys of a transition metal dichalcogenide (TMD) monolayer strongly coupled to a plasmonic OSO resonator, at room temperature (RT). In this strong coupling regime, each spin-polarized valley exciton is hybridized with a single mode plasmon of specific momentum. The chiral nature of this interaction generates spin-momentum locked polaritonic states, which we will refer to with the portmanteau *chiralitons*. A striking feature of our platform is its capacity to induce RT robust valley contrasts, enabling the directional transport of chiralitons over micron scale distances. Moreover, these polaritons yield long lived coherences that we experimentally measure, demonstrating the generation of entangled counter propagating chiralitonic flows. These results, unexpected from the bare TMD monolayer RT properties [15–17], point towards the importance of the strong coupling regime where the excitonic disorder is spatially averaged by the delocalized nature of the polaritonic states [18, 19].

The small Bohr radii and reduced screening of monolayer TMD excitons provide the extremely large oscillator strength required for light matter interaction in the strong coupling regime, as already achieved in Fabry-Pérot cavities [20–22] and more recently in plasmonic resonators [23, 24]. In this context, Tungsten Disulfide (WS_2) naturally sets itself as a perfect material for RT strong coupling [24] due to its sharp and intense A-exciton absorption peak, well separated from the higher energy B-exciton line (see Fig. 1(a)) [25]. Moreover, the inversion symmetry breaking of the crystalline order on a TMD monolayer, combined with time-reversal symmetry, leads to spin-polarized valley transitions at the K and K' points of the associated Brillouin zone, as sketched in Fig. 1(b) [26]. This polarization property makes therefore atomically thin TMD semiconductors very promising candidates with respect to the chiral aspect of the coupling between the excitonic valleys and the plasmonic OSO modes, resulting in the energy diagram shown in Fig. 1(c).

Experimentally, our system, shown in Fig. 2(a), consists of a mechanically exfoliated monolayer of WS_2 covering a plasmonic OSO hole array, with a 5 nm thick dielectric spacer (polymethyl methacrylate). The array, imaged in Fig. 2(b), is designed on a (x, y) square lattice with a grating period Λ, and consists of rectangular nano-apertures (160×90 nm^2) rotated stepwise along the x-axis by an angle $\phi = \pi/6$. The associated orbital period $6 \times \Lambda$ sets a rotation vector $\mathbf{\Omega} = (\phi/\Lambda)\hat{z}$, which combines with the spin σ of the incident light into a geometric phase $\Phi_g = -\Omega\sigma x$ [27]. The gradient of this geometric phase imparts a momentum $\mathbf{k}_g = -\sigma(\phi/\Lambda)\hat{x}$ contributing to the matching condition on the array between the plasmonic $\mathbf{k}_{\mathrm{SP}}$ and incidence in-plane $\mathbf{k}_{\mathrm{in}}$ momenta: $\mathbf{k}_{\mathrm{SP}} = \mathbf{k}_{\mathrm{in}} + (2\pi/\Lambda)(n\hat{x} + m\hat{y}) + \mathbf{k}_g$. This condition defines different (n, m) orders for the plasmonic dispersions, which are transverse magnetic (TM) and transverse electric (TE) polarized along the x and y axis of the array

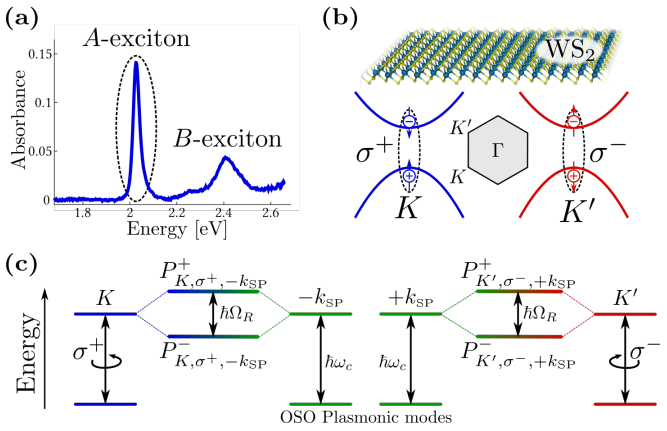

FIG. 1. (a) Absorbance spectrum of a WS_2 monolayer as obtained from its transmission spectrum. (b) Crystal packing of a tungsten disulfide (WS_2) monolayer, and sketch of its electronic band structure around the points K and K' of the Brillouin zone, with the corresponding optical selection rules for band-edge excitons formation under left (σ^+) and right (σ^-) circular excitation. (c) Energy level diagram of the K and K' excitons of WS_2 strongly coupled to an OSO plasmonic mode at energy $\hbar\omega_c$ and wavevector $\pm k_{SP}$.

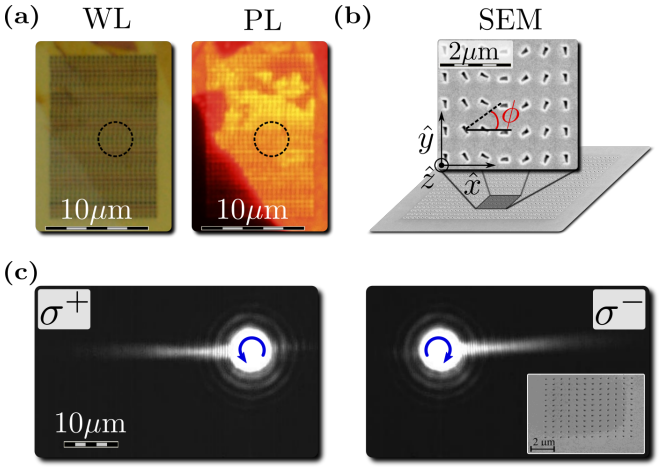

FIG. 2. (a) White light (WL) microscope image of the sample and photoluminescence (PL) image of the same area under 2.58 eV excitation. (b) SEM image of the plasmonic OSO resonator fabricated by sputtering 200 nm of gold on a glass substrate coated by a 5 nm thick chromium adhesion layer. The array with ϕ-rotated rectangular apertures is milled through the metallic layers using a focused ion beam (FIB). (c) Real-space leakage radiation microscope [9] images of the surface plasmons launched by σ^+ and σ^- excitations on a OSO plasmonic resonator similar to the one of panel (b).

respectively (see Fig. 2(b)). It is important to note that the contribution of the geometric phase impacts the TM dispersions only. The period of our structure $\Lambda = 480$ nm is optimized to have $n = +1$ and $n = -1$ TM modes resonant with the absorption energy of the A-exciton of WS_2 at 2.01 eV for σ^+ and σ^- illuminations respectively. This strict relation between $n = \pm 1$ and $\sigma = \pm 1$ is the OSO mechanism that breaks the left vs. right symmetry of the modal response of the array, which in this sense becomes chiral. Plasmon modes are thus launched in counter-propagating directions along the x-axis for opposite spins σ of the excitation light. In the case of a bare plasmonic OSO resonator, this is clearly observed in Fig. 2(c). We stress that similar arrangements of anisotropic apertures have previously been demonstrated to allow for spin-dependent surface plasmon launching [7, 9, 28, 29].

Angle-resolved white light reflectometries of the whole structure (Fig. 2(a)) are shown in Fig. 3 (a) and (b) for left and right circular polarizations. In each case, two strongly dispersing branches are observed, featuring a clear anti-crossing behavior. This demonstrates that the system is in the strong coupling regime, with the two branches corresponding to upper and lower chiralitonic states. This is further confirmed by a coupled oscillators fit to the dispersions, giving a Rabi splitting of 40 meV, close to our previous observations on non-OSO plasmonic resonators [24]. The two dispersion diagrams show a clear mirror symmetry breaking with respect to the normal incident axis ($k_x = 0$) for the two opposite optical spins. This clearly demonstrates the capability of our structure to act as a spin-momentum locked polariton launcher.

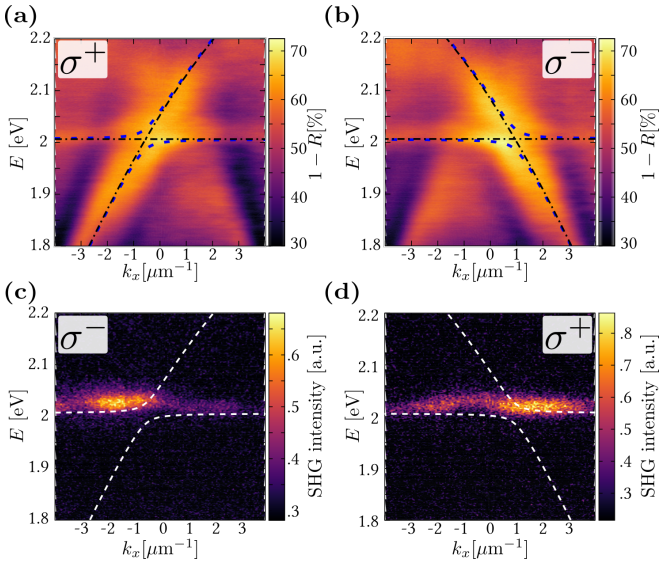

FIG. 3. Angle-resolved reflectivity spectrum of the sample analysed in (a) left and (b) right circular polarization. Angle-resolved resonant second harmonic spectrum for (c) right and (d) left circular excitation at 1.01eV.

From the linewidth and the curvature of the dispersion relations, we can estimate a chiraliton propagation length in the micrometer range, in good agreement with the measured PL extent presented in the Supplemental Material (see Sec. A, [30]).

In view of chiral light-chiral matter interactions, we further investigate the interplay between this plasmonic

chirality and the valley-contrasting chirality of the WS_2 monolayer. A first demonstration of such an interplay is found in the resonant second harmonic (SH) response of the strongly coupled system. Indeed, monolayer TMDs have been shown to give a high valley contrast in the generation of a SH signal resonant with their A-excitons [31]. As we show in Supplemental Material Sec. B [30] such high SH valley contrast are measured on a bare WS_2 monolayer. The optical selection rules for SH generation are opposite to those found in linear absorption since the process involves two excitation photons, and are more robust since the SH process is instantaneous. The angle resolved resonant SH signals are shown in Fig. 3(c) and (d) for left and right circularly polarized excitation, respectively. These results show a very good agreement with the dispersion features observed in reflectometry for opposite circular polarizations (Fig. 3(a) and (b) respectively). As expected, the left vs. right contrast measured on the SH signal (ca. 20%) is close to the one measured on the reflectometry maps (ca. 15%). This unambigously demonstrates the selective coupling of excitons in one valley to surface plasmons propagating in one direction, thus realizing valley-contrasting chiralitonic states with spins locked to their propagation wavevectors:

$$|P^{\pm}_{K,\sigma^+,-k_{\rm SP}}>=|g_K,1_{\sigma^+},-k_{\rm SP}>\pm|e_K,0_{\sigma^+},-k_{\rm SP}>$$
$$|P^{\pm}_{K',\sigma^-,+k_{\rm SP}}>=|g_{K'},1_{\sigma^-},+k_{\rm SP}>\pm|e_{K'},0_{\sigma^-},+k_{\rm SP}>,$$

where $e_i(g_i)$ corresponds to the presence (absence) of an exciton in the valley $i=(K,K')$ of WS_2, and $1_j(0_j)$ to 1 (0) plasmon in the mode of polarization $j=(\sigma^+,\sigma^-)$ and wavevector $\pm k_{\rm SP}$. Importantly, while in a weakly coupled system the spin-dependent SH signal would be localized at the exciton-plasmon crossing points, here we observe extended features spanning a large k_x range of the dispersion diagram. This stems from the hybrid structure of the chiralitonic states, with the valley contrast of WS_2 and the spin-locking property of the OSO plasmonic resonator being imprinted on the new eigenstates of the system. These observations constitute an indisputable proof that our system does indeed operate in the strong coupling regime.

The spin-locking property of chiralitonic states, as revealed by the resonant SH measurements, incurs however different relaxation mechanisms through the dynamical evolution of the chiralitons. In particular, excitonic intervalley scattering can erase valley contrast in WS_2 at RT [32] -see below. In our configuration, this would transfer chiraliton population from one valley to the other, generating via optical spin-locking, a reverse flow, racemizing the chiraliton population. This picture however does not account for the possibility of more robust valley contrasts in strong coupling conditions, as recently reported with $MoSe_2$ in Fabry-Pérot cavities [19]. The chiralitonic flow is measured by performing angle resolved polarized PL experiments, averaging the signal over the PL lifetime of ca. 200 ps (see Supplemental Material, Sec. C and D [30]). For these experiments, the laser excitation energy is chosen at 1.96 eV, slightly below the WS_2 bandgap. At this energy, the measured PL results from an phonon-induced up-convertion process [33]. The difference between PL dispersions obtained with left and right circularly polarized excitations is displayed in Fig. 4(a), showing net flows of chiralitons with spin-determined momenta. This is in clear agreement with the differential white-light reflectivity map $R_{\sigma^-}-R_{\sigma^+}$ of Fig. 4(b). Considering that this map gives the sorting efficiency of our OSO resonator, such correlations in the PL implies that the initial spin-momentum determination of the chiralitons (see Fig. 3 (c) and (d)) survives over 200 ps at RT. After this PL lifetime, a net chiral flow $\mathcal{F}=I_{\sigma^-}-I_{\sigma^+}$ of $\sim 6\%$ is extracted from Fig. 4 (a). This corresponds to a chiralitonic valley polarization, in striking contrast with the absence of valley polarization that we report for a bare WS_2 monolayer at RT in the Supplemental Material, Sec. E [30]. The extracted net flow is however limited by the actual finite optical contrast $\mathcal{C}$ of our OSO resonator, which we measure at a 15% level from a cross-cut taken on Fig. 4 (b) at 1.98 eV. It is therefore possible to infer that a chiralitonic valley contrast of $\mathcal{F}/\mathcal{C}\simeq 40\%$ can be reached at RT for the strongly coupled WS_2 monolayer. As mentioned above, this surprisingly robust contrast, only observed on our strongly coupled system, could be seen a consequence of the local excitonic disorder averaging performed by the propagating chiralitons, in analogy with what has been observed on other polaritonic systems [18, 19].

As a consequence of this motional narrowing effect, such a strongly coupled system involving atomically thin crystals of TMDs could then provide new ways to incorporate intervalley coherent dynamics [15, 17, 34–36] into the realm of polariton physics. To illustrate this, we now show that two counter-propagating flows can evolve coherently, leading to the generation of entangled chiraliton pairs:

$$|\Psi>=|P^{\pm}_{K,\sigma^+,-k_{\rm SP}}>+|P^{\pm}_{K',\sigma^-,+k_{\rm SP}}>. \qquad (1)$$

Intervalley coherence is expected to result in a non-zero degree of linearly polarized PL when excited by the same linear polarization. This can be monitored by measuring the $S_1=I_{\rm TM}-I_{\rm TE}$ coefficient of the PL Stokes vector, where $I_{\rm TM(TE)}$ is the emitted PL intensity analyzed in TM (TE) polarization. This coefficient is displayed in the k_x-energy plane in Fig. 4(c) for an incident TM polarized excitation at 1.96 eV. Fig. 4(e) displays the same coefficient under TE excitation. A clear polarization anisotropy on the chiraliton emission is observed for both TM and TE excitation polarizations, both featuring the same symmetry along the $k_x=0$ axis as the differential reflectivity dispersion map $R_{\rm TM}-R_{\rm TE}$ shown in Fig. 4(d). As detailed in the Supplemental Material (Sec. F [30]), the degree of chiralitonic intervalley coherence can be directly quanti-

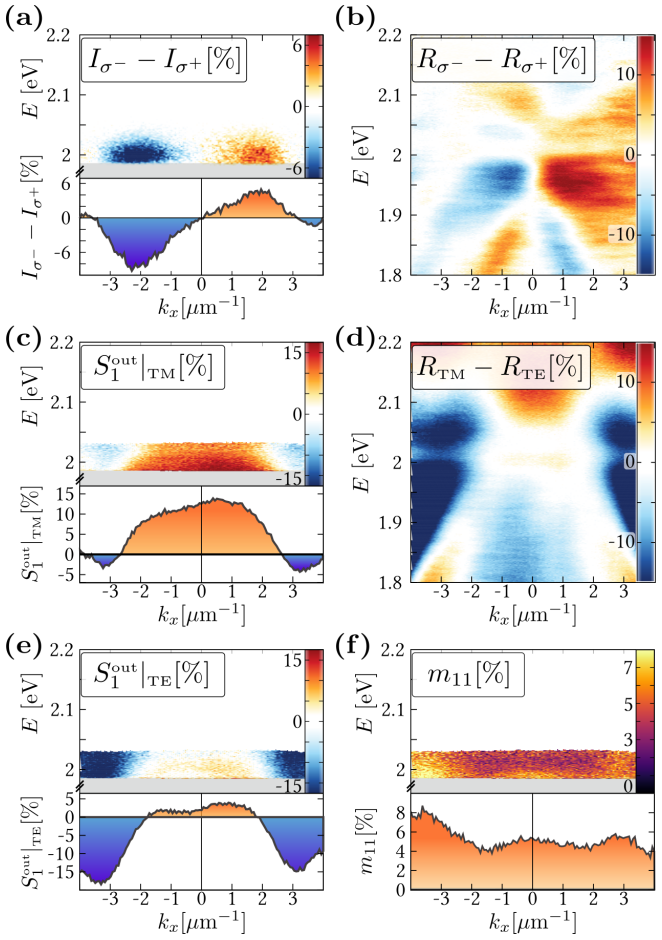

FIG. 4. (a) Differential PL dispersion spectrum for left and right circularly polarized excitations. The shaded regions in all panels are removed by the laser line filter, and the cross-cuts are taken at 2 eV. (b) Differential angle-resolved reflection spectrum for left and right circularly polarized light. (c), (e) Angle-resolved spectrum of the normalized coefficient $S_1^{out}|_{TM(TE)}/S_0$ of the PL Stokes vector for a TM(TE) polarized excitation (see text for details). Note that we have put a detection threshold below 100 photon counts that cuts the signal above ~ 2.03 eV in panels (a), (c), (e) and (f). (d) Differential angle-resolved reflection spectrum obtained from analyzed TM and TE measurements. (f) k_x-energy dispersion of the degree of chiralitonic inter-valley coherence m_{11} computed from (c) and (e).

fied by the difference $S_1^{out}|_{TM} - S_1^{out}|_{TE}$, which measures the PL linear depolarization factor displayed (as m_{11}) in Fig. 4 (f). By this procedure, we retrieve a chiralitonic intervalley coherence that varies between 5% and 8% depending on k_x. Interestingly, these values that we reach at RT have magnitudes comparable than those reported on a bare WS_2 monolayer at 10 K [37]. This unambiguously shows how such strongly coupled TMD systems can sustain RT coherent dynamics over long lifetimes and propagation distances.

In summary, we demonstrate valley contrasting spin-momentum locked chiralitonic states in an atomically thin TMD semiconductor strongly coupled to a plasmonic OSO resonator. The survival of such contrasts over 200 ps lifetimes is made possible by the unexpectedly robust RT coherences inherent to the strong coupling regime. Exploiting such long-lived coherences, we measure chiralitonic flows that can evolve in entangled superpositions over micron scale distances. Our results show that the combination of OSO interactions with TMD valleytronics is an interesting path to follow in order to explore and manipulate RT coherences in chiral quantum architectures [38].

This work was supported in part by the ANR Equipex "Union" (ANR-10-EQPX-52-01), ANR Grant (H2DH ANR-15-CE24-0016), the Labex NIE projects (ANR-11-LABX-0058-NIE) and USIAS within the Investissement d'Avenir program ANR-10-IDEX-0002-02. Y. G. acknowledges support from the Ministry of Science, Technology and Space, Israel. S. B. is a member of the Institut Universitaire de France (IUF).

Author Contributions - T. C. and S. A. contributed equally to this work.

[1] K. Y. Bliokh, F. Rodríguez-Fortuño, F. Nori, and A. V. Zayats, Nat. Photon. **9**, 796 (2015).
[2] Z. Bomzon, G. Biener, V. Kleiner, and E. Hasman, Opt. Lett. **27**, 1141 (2002).
[3] B. le Feber, N. Rotenberg, and L. Kuipers, Nat. Comm. **6**, 6695 (2015).
[4] J. Petersen, J. Volz, and A. Rauschenbeutel, Science **346**, 67 (2014).
[5] M. Rafayelyan, G. Tkachenko, and E. Brasselet, Phys. Rev. Lett. **116**, 253902 (2016).
[6] Y. Gorodetski, A. Drezet, C. Genet, and T. W. Ebbesen, Phys. Rev. Lett. **110**, 203906 (2013).
[7] J. Lin, J. B. Mueller, Q. Wang, G. Yuan, N. Antoniou, X.-C. Yuan, and F. Capasso, Science **340**, 331 (2013).
[8] F. J. Rodríguez-Fortuño, G. Marino, P. Ginzburg, D. O'Connor, A. Martínez, G. A. Wurtz, and A. V. Zayats, Science **340**, 328 (2013).
[9] Q. Jiang, A. Pham, M. Berthel, S. Huant, J. Bellessa, C. Genet, and A. Drezet, ACS Photon. **3**, 1116 (2016).
[10] D. O'Connor, P. Ginzburg, F. J. Rodríguez-Fortuño, G. A. Wurtz, and A. V. Zayats, Nat. Comm. **5**, 5327 (2014).
[11] R. Mitsch, C. Sayrin, B. Albrecht, P. Schneeweiss, and A. Rauschenbeutel, Nat. Comm. **5**, 5713 (2014).
[12] C. Sayrin, C. Junge, R. Mitsch, B. Albrecht, D. O'Shea, P. Schneeweiss, J. Volz, and A. Rauschenbeutel, Phys. Rev. X **5**, 041036 (2015).
[13] I. Söllner, S. Mahmoodian, S. L. Hansen, L. Midolo, A. Javadi, G. Kiršanskė, T. Pregnolato, H. El-Ella, E. H. Lee, J. D. Song, S. Stobbe, and P. Lodahl, Nat. Nano. **10**, 775 (2015).
[14] P. Lodahl, S. Mahmoodian, S. Stobbe, P. Schneeweiss, J. Volz, A. Rauschenbeutel, H. Pichler, and P. Zoller, Nature **541**, 473 (2017).

[15] A. M. Jones, H. Yu, N. J. Ghimire, S. Wu, G. Aivazian, J. S. Ross, B. Zhao, J. Yan, D. G. Mandrus, D. Xiao, W. Yao, and X. Xu, Nat. Nano. **8**, 634 (2013).

[16] G. Moody, J. Schaibley, and X. Xu, J. Opt. Soc. Am. B **33**, C39 (2016).

[17] K. Hao, G. Moody, F. Wu, C. K. Dass, L. Xu, C.-H. Chen, L. Sun, M.-Y. Li, L.-J. Li, A. H. MacDonald, and X. Li, Nat. Phys. **Advance Online Publication** (2016), 10.1038/nphys3674.

[18] D. M. Whittaker, P. Kinsler, T. A. Fisher, M. S. Skolnick, A. Armitage, A. M. Afshar, M. D. Sturge, and J. S. Roberts, Phys. Rev. Lett. **77**, 4792 (1996).

[19] S. Dufferwiel, T. P. Lyons, D. D. Solnyshkov, A. A. P. Trichet, F. Withers, S. Schwarz, G. Malpuech, J. M. Smith, K. S. Novoselov, M. S. Skolnick, D. N. Krizhanovskii, and A. I. Tartakovskii, (2016), arXiv:1612.05073 [cond-mat.mes-hall].

[20] X. Liu, T. Galfsky, Z. Sun, F. Xia, E.-C. Lin, Y.-H. Lee, S. Kéna-Cohen, and V. M. Menon, Nat. Photon. **9**, 30 (2015).

[21] S. Dufferwiel, S. Schwarz, F. Withers, A. A. P. Trichet, F. Li, M. Sich, O. Del Pozo-Zamudio, C. Clark, A. Nalitov, D. D. Solnyshkov, G. Malpuech, K. S. Novoselov, J. M. Smith, M. S. Skolnick, D. N. Krizhanovskii, and A. I. Tartakovskii, Nat. Comm. **6**, 8579 (2015).

[22] M. Sidler, P. Back, O. Cotlet, A. Srivastava, T. Fink, M. Kroner, E. Demler, and A. Imamoğlu, Nat. Phys. **advance online publication** (2016), 10.1038/nphys3949.

[23] W. Liu, B. Lee, C. H. Naylor, H.-S. Ee, J. Park, A. T. C. Johnson, and R. Agarwal, Nano Lett. **16**, 1262 (2016).

[24] S. Wang, S. Li, T. Chervy, A. Shalabney, S. Azzini, E. Orgiu, J. A. Hutchison, C. Genet, P. Samorì, and T. W. Ebbesen, Nano Lett. **16**, 4368 (2016).

[25] Y. Li, A. Chernikov, X. Zhang, A. Rigosi, H. M. Hill, A. M. van der Zande, D. A. Chenet, E.-M. Shih, J. Hone, and T. F. Heinz, Phys. Rev. B **90**, 205422 (2014).

[26] K. F. Mak and J. Shan, Nat. Photon. **10**, 216 (2016).

[27] K. Y. Bliokh, Y. Gorodetski, V. Kleiner, and E. Hasman, Phys. Rev. Lett. **101**, 030404 (2008).

[28] N. Shitrit, I. Bretner, Y. Gorodetski, V. Kleiner, and E. Hasman, Nano Lett. **11**, 2038 (2011).

[29] L. Huang, X. Chen, B. Bai, Q. Tan, G. Jin, T. Zentgraf, and S. Zhang, Light Sci. Appl. **2** (2013), 10.1038/lsa.2013.26.

[30] See Supplemental Material for detailed descriptions of the measurements of the polariton diffusion length, the SH valley contrast, the PL lifetime of the strongly coupled system, the valley contrast of bare WS_2 monolayer, the angle resolved PL polarimetry.

[31] K. L. Seyler, J. R. Schaibley, P. Gong, P. Rivera, A. M. Jones, S. Wu, J. Yan, D. G. Mandrus, W. Yao, and X. Xu, Nat. Nano. **10**, 407 (2015).

[32] A. T. Hanbicki, K. M. McCreary, G. Kioseoglou, M. Currie, C. S. Hellberg, A. L. Friedman, and B. T. Jonker, AIP Advances **6**, 055804 (2016), http://dx.doi.org/10.1063/1.4942797.

[33] A. M. Jones, H. Yu, J. R. Schaibley, J. Yan, D. G. Mandrus, T. Taniguchi, K. Watanabe, H. Dery, W. Yao, and X. Xu, Nat. Phys. **12**, 323 (2016).

[34] G. Wang, X. Marie, B. L. Liu, T. Amand, C. Robert, F. Cadiz, P. Renucci, and B. Urbaszek, Phys. Rev. Lett. **117**, 187401 (2016).

[35] R. Schmidt, A. Arora, G. Plechinger, P. Nagler, A. Granados del Aguila, M. V. Ballottin, P. C. M. Christianen, S. Michaelis de Vasconcellos, C. Schuller, T. Korn, and R. Bratschitsch, Phys. Rev. Lett. **117**, 077402 (2016).

[36] Z. Ye, D. Sun, and T. F. Heinz, Nat. Phys. **13**, 26 (2017).

[37] B. Zhu, H. Zeng, J. Dai, Z. Gong, and X. Cui, PNAS **111**, 11606 (2014).

[38] T. Low, A. Chaves, J. D. Caldwell, A. Kumar, N. X. Fang, P. Avouris, T. F. Heinz, F. Guinea, L. Martin-Moreno, and F. Koppens, Nat. Mater. **16**, 182 (2017).

[39] F. Federspiel, G. Froehlicher, M. Nasilowski, S. Pedetti, A. Mahmood, B. Doudin, S. Park, J.-O. Lee, D. Halley, B. Dubertret, P. Gilliot, and S. Berciaud, Nano Lett. **15**, 1252 (2015).

[40] P. K. Nayak, F.-C. Lin, C.-H. Yeh, J.-S. Huang, and P.-W. Chiu, Nanoscale **8**, 6035 (2016).

SUPPLEMENTAL MATERIAL: SPIN-MOMENTUM LOCKED POLARITON TRANSPORT IN CHIRAL STRONG COUPLING REGIME

A: Chiraliton diffusion length

The diffusion length of chiralitons can be estimated by measuring the extent of their photoluminescence (PL) under a tightly focused excitation. To measure this extent, we excite a part of a WS_2 monolayer located above the plasmonic hole array (Fig. S5(a) and (b)). This measurement is done on a home-built PL microscope, using a 100× microscope objective of 0.9 numerical aperture and exciting the PL with a HeNe laser at 1.96 eV, slightly below the exciton band-gap. A diffraction-limited spot of 430 nm half-width is obtained Fig. S5(c)) by bringing the sample in the focal plane of the microscope while imaging the laser beam on a Peltier-cooled CCD camera. The PL is collected by exciting at 10 μW of optical power, and is filtered from the scattered laser light by a high-energy-pass filter. The resulting PL image is shown in Fig. S5(d), clearly demonstrating the propagating character of the emitting chiralitons. The logarithmic cross-cuts (red curves in (c) and (d)) reveal a propagation length of several microns.

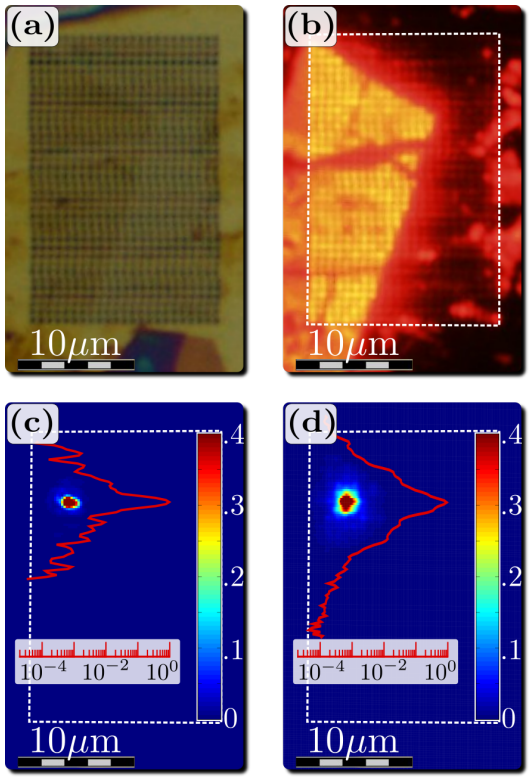

FIG. 5. (a) White light image of a WS_2 flake covering the plasmonic hole array, and (b) its wide field PL. (c) Normalized image of the diffraction-limited laser spot on the structure (indicated by the white dashed rectangle in (c) and (d)). The logarithmic scale cross-cuts (red curves in (c) and (d)) are taken along the vertical axis, through the intensity maximum. (d) Normalized chiraliton PL image.

B: Resonant Second Harmonic generation on a WS_2 monolayer

As discussed in the main text, TMD monolayers have recently been shown to give a high valley contrast in the generation of a second harmonic (SH) signal resonant with their *A*-excitons. We obain a similar result when measuring a part of the WS_2 monolayer sitting above the bare metallic surface, i.e. aside from the plasmonic hole array. In Fig. S6 we show the SH signal obtained in left and right circular polarization for an incident femtosecond pump beam (120 fs pulse duration, 1 kHz repetition rate at 1.01 eV) in (a) left and (b) right circular polarization. This result confirms that the SH signal polarization is a good observable of the valley degree of freedom of the WS_2 monolayer, with a contrast reaching ca. 80%. In Fig. 3(c) and (d) of the main text, we show how this valley state is imprinted on the chiralitonic states.

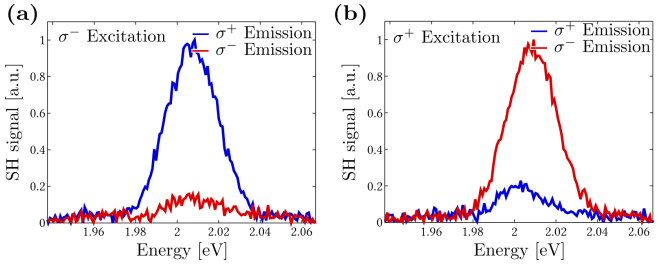

FIG. 6. Resonant SH spectrum for left and right circular analysis, for (a) left and (b) right circular excitation at 1.01eV.

C: PL lifetime measurement on the strongly coupled system

The PL lifetime of the strongly coupled system is measured by time-correlated single photon counting (TCSPC) under pico-second pulsed excitation (instrument response time 120 ps, 20 MHz repetition rate at 1.94 eV). The arrival time histogram of PL photons, when measuring a part of the WS_2 monolayer located above the plasmonic hole array, gives the decay dynamic shown in Fig. S7(a). On this figure we also display the PL decay of a reference WS_2 monolayer exfoliated on a dielectric substrate (polydimethylsiloxane), as well as the instrument response function (IRF) measured by recording the excitation pulse photons scattered by a gold film. Following the procedure detailed in [39], we define the *calculated* decay times τ_{calc} as the area under the de-

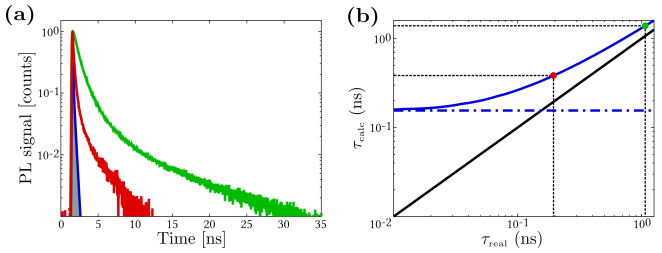

FIG. 7. (a) TCSPC histogram showing the PL decay dynamic of the strongly coupled WS_2 monolayer (red curve), as compared to that of a bare WS_2 monolayer on a dielectric substrate (green curve). The IRF of our measurement apparatus is shown in blue. (b) Calibration (blue curve) used to retrieve $\tau_{\rm real}$ from the measurement of $\tau_{\rm calc}$, obtained by convoluting an exponential decay of time constant $\tau_{\rm real}$ with the measured IRF. The calculated IRF time constant $\tau_{\rm calc}^{\rm IRF} = 157$ ps is shown by the blue dashed line. $\tau_{\rm calc}^{\rm ref}$ and $\tau_{\rm calc}^{\rm sample}$ are represented as green and red spots respectively.

cay curves (corrected for their backgrounds) divided by their peak values. This yields a calculated IRF time constant $\tau_{\rm calc}^{\rm IRF} = 157$ ps, and calculated PL decay constants $\tau_{\rm calc}^{\rm ref} = 1.39$ ns and $\tau_{\rm calc}^{\rm sample} = 384$ ps for the reference bare flake and the strongly coupled sample respectively. The *real* decay time constants $\tau_{\rm real}$ corresponding to the calculated ones can then be estimated by convoluting different monoexponential decays with the measured IRF, computing the corresponding $\tau_{\rm calc}$ and interpolating this calibration curve (Fig. S6(b)) for the values of $\tau_{\rm calc}^{\rm ref}$ and $\tau_{\rm calc}^{\rm sample}$. This results in $\tau_{\rm real}^{\rm ref} = 1.06$ ns and $\tau_{\rm real}^{\rm sample} = 192$ ps.

D: Optical setup

The optical setup used for PL polarimetry experiments is shown in Fig. S8. The WS_2 monolayer is excited by a continous-wave HeNe laser at 1.96 eV (632 nm), slightly below the direct band-gap of the atomic crystal, in order to reduce phonon-induced valley depolarization effects at room temperature. The pumping laser beam is filtered by a bandpass filter (BPF) and its polarization state is controlled by a set of polarization optics: a linear polarizer (LP), a half-wave plate (HWP) and a quarter-wave plate (QWP). The beam is focused onto the sample surface at oblique incidence angle by a microscope objective, to a typical spot size of 100 μm^2. This corresponds to a typical flux of 10 W·cm^{-2}. In such conditions of irradiation, the PL only comes from the $A-$exciton. The isotropically-emitted PL signal is collected by a high numerical aperture objective, and its polarization state is analyzed by another set of broadband polarization optics (HWP, QWP, LP). A short-wavelength-pass (SWP) tunable filter is placed on the optical path to stop the laser light scattered. Adjustable slits (AS) placed at the image plane of the tube lens (TL) allow to spatially select the

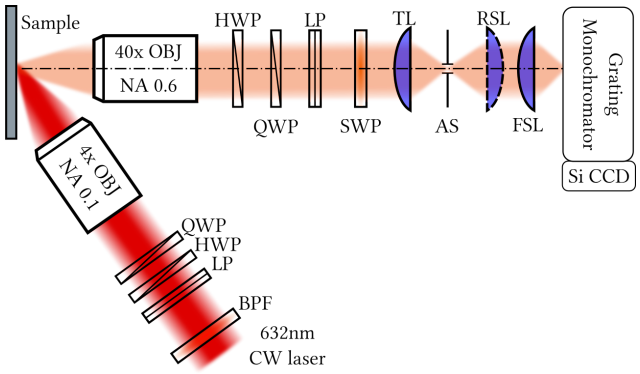

FIG. 8. Optical setup used for the angle-resolved polarimetric measurements. See the corresponding paragraph for details.

PL signal coming only from a desired area of the sample, whose Fourier-space (or real space) spectral content can be imaged onto the entrance slits of the spectrometer by a Fourier-space lens (FSL), or adding a real-space lens (RSL). The resulting image is recorded by a cooled CCD Si camera.

E: Valley contrast measurements on a bare WS_2 monolayer

The valley contrast $\rho^{\pm}$ of a bare WS_2 monolayer exfoliated on a dielectric substrate (polydimethylsiloxane) is computed from the measured room temperature PL spectra obtained for left and right circular excitations, analysed in the circular basis by a combination of a quarter-wave plate and a Wollaston prism:

$$\rho^{\pm} = \frac{I_{\sigma^{\pm}}(\sigma^+) - I_{\sigma^{\pm}}(\sigma^-)}{I_{\sigma^{\pm}}(\sigma^+) + I_{\sigma^{\pm}}(\sigma^-)}, \qquad (2)$$

where $I_j(l)$ is the measured PL spectrum for a $j = (\sigma^+, \sigma^-)$ polarized excitation and a $l = (\sigma^+, \sigma^-)$ polarized analysis. A typical emission spectrum ($I_{\sigma^-}(\sigma^-)$) is shown in Fig. S9(a) and the valley contrasts $\rho^{\pm}$ are displayed in Fig. S9(b). As discussed in the main text, this emission spectrum consists of a phonon-induced upconverted PL [33]. Clearly, there is no difference in the $I_j(l)$ spectra, hence no valley polarization at room temperature on the bare WS_2 monolayer. These results are in striking contrast to those reported in the main text for the strongly coupled system, under similar excitation conditions. Note also that the absence of valley contrast on our bare WS_2 monolayer differs from the results of [40] reported however on WS_2 grown by chemical vapor deposition.

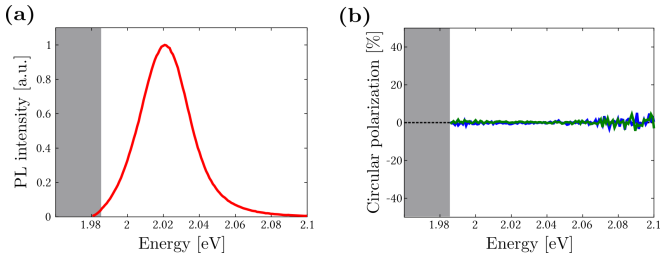

FIG. 9. (a) Emission spectrum $I_{\sigma^-}(\sigma^-)$ obtained by exciting the bare WS_2 monolayer at 1.96 eV with σ^- polarized light, and analysing the PL in σ^- polarization. The gray area in (a) and (b) corresponds to the spectral region cut by the PL emission filter. (b) The CPL contrast $\rho^{+(-)}$ defined in (2) is displayed in blue (green).

F: Angle-resolved Stokes vector polarimetry

The optical setup shown in Fig. S8 is used to measure the angle-resolve PL spectra for different combinations of excitation and detection polarizations. Such measurements allow us to retrieve the coefficients of the Mueller matrix $\mathcal{M}$ of the system, characterizing how the polarization state of the excitation beam affects the polarization state of the chiralitons PL. As discussed in the main text, the spin-momentum locking mechanism of our chiralitonic system relates such PL polarization states to specific chiraliton dynamics. An incident excitation in a given polarization state is defined by a Stokes vector $\mathbf{S}^{\text{in}}$, on which the matrix $\mathcal{M}$ acts to yield an output PL Stokes vector $\mathbf{S}^{\text{out}}$:

$$\mathbf{S}^{\text{out}} = \begin{pmatrix} I \\ I_V - I_H \\ I_{45} - I_{-45} \\ I_{\sigma^+} - I_{\sigma^-} \end{pmatrix}_{\text{out}} = \mathcal{M} \begin{pmatrix} I_0 \\ I_V - I_H \\ I_{45} - I_{-45} \\ I_{\sigma^+} - I_{\sigma^-} \end{pmatrix}_{\text{in}}, \quad (3)$$

where $I_{(0)}$ is the emitted (incident) intensity, $I_V - I_H$ is the relative intensity in vertical and horizontal polarizations, $I_{45} - I_{-45}$ is the relative intensity in $+45^o$ and -45^o polarizations and $I_{\sigma^+} - I_{\sigma^-}$ is the relative intensity in σ^+ and σ^- polarizations. We recall that for our specific alignment of the OSO resonator with respect to the slits of the spectrometer, the angle-resolved PL spectra in V and H polarizations correspond to transverse-magnetic (TM) and transverse-electric (TE) dispersions respectively (see Fig. 2(b) of the main text). Intervalley chiraliton coherences, revealed by a non-zero degree of linear polarization in the PL upon the same linear excitation, are then measured by the $S_1 = I_V - I_H$ coefficient of the PL output Stokes vector. This coefficient is obtained by analysing the PL in the linear basis, giving an angle-resolved transmitted PL intensity $\left(S_0^{\text{out}} + (-)S_1^{\text{out}}\right)/2$, for TM (TE) analysis. In order to obtain intrinsic polarization characteristics of the chiralitons, we measure the four possible combinations of excitation and detection polarization in the linear basis:

$$I_{\text{TM/TM}} = (m_{00} + m_{01} + m_{10} + m_{11})/2 \quad (4)$$
$$I_{\text{TM/TE}} = (m_{00} + m_{01} - m_{10} - m_{11})/2 \quad (5)$$
$$I_{\text{TE/TM}} = (m_{00} - m_{01} + m_{10} - m_{11})/2 \quad (6)$$
$$I_{\text{TE/TE}} = (m_{00} - m_{01} - m_{10} + m_{11})/2, \quad (7)$$

where $I_{p/a}$ is the angle-frequency resolved intensity measured for a pump polarization p = (TE,TM) and analysed in a = (TE,TM) polarization, and $m_{i,j}$ are the coefficients of the 4x4 matrix $\mathcal{M}$. By solving this linear system of equations, we obtain the first quadrant of the Mueller matrix: m_{00}, m_{01}, m_{10} and m_{11}. The $S_1^{\text{out}}|_{\text{TM}}$ coefficient of the output Stokes vector for a TM excitation is then directly given by $m_{10} + m_{11}$ as can be seen from (3) by setting $I_V = 1, I_H = 0$ and all the other input Stokes coefficients to zeros. This quantity, normalized to S_0^{out}, is displayed in the k_x-energy plane in Fig. 4(c) of the main text. Similarly, the $S_1^{\text{out}}|_{\text{TE}}$ coefficient is given by $m_{10} - m_{11}$, which is the quantity displayed in Fig. 4(d) of the main text.

As the dispersion of the OSO resonator is different for TE and TM polarizations, the pixel-to-pixel operations performed to obtain S_1^{out} do not directly yield the chiraliton inter-valley contrast. In particular, the observation of negative value regions in $S_1^{\text{out}}|_{\text{TM}}$ only reveals that the part of the chiraliton population that lost inter-valley coherence is dominating the total PL in the region of the dispersion where the TE mode dominates over the TM mode (compare Fig. 4(c) and (e)). It *does not* correspond to genuine anti-correlation of the chiraliton PL polarization with respect to the pump polarization. To correct for such dispersive effects and obtain the degree of chiraliton intervalley coherence, the appropriate quantity is $(S_1^{\text{out}}|_{\text{TM}} - S_1^{\text{out}}|_{\text{TE}})/(2S_0^{\text{out}}) = m_{11}$, resolved in the k_x-energy plane in Fig. 4(f) of the main text. This quantity can also be refered to as a chiraliton linear depolarization factor. For all these polarimetry measurements, we stress that the noise level is below 0.1%.